Applied Physics A (2023) 129:754
https://doi.org/10.1007/s00339-023-07032-y

Applied Physics A
Materials Science & Processing

High surface area g-C_3N_4 nanosheets as superior solar-light photocatalyst for the degradation of parabens

S. Stefa[1,2] · M. Zografaki[1] · M. Dimitropoulos[3,4] · G. Paterakis[3,4] · C. Galiotis[3,4] · P. Sangeetha[6] · G. Kiriakidis[1] · M. Konsolakis[2] · V. Binas[1,5,7]

Received: 11 May 2023 / Accepted: 25 September 2023 / Published online: 11 October 2023

Abstract

The rational design and development of highly-active photocatalytic materials for the degradation of dangerous chemical compounds, such as parabens, is one of the main research pillars in the field of photocatalysis. Graphitic carbon nitride (g-C_3N_4) is a 2D non-metal material and is considered one of the most promising photocatalysts, because of its peculiar physicochemical properties. In this work, porous g-C_3N_4 nanosheets (CNNs) were successfully prepared via thermal exfoliation of bulk g-C_3N_4 (CNB). A thorough physicochemical characterization analysis before and after the exfoliation process was performed, revealing the improved textural characteristics (surface area of 212 m^2/g), chemical stability, and optical properties (wide band gap of 2.91 eV) of CNNs compared to the CNB. Then, both CNB and CNNs were comparatively assessed as photocatalysts for the degradation of methyl-, ethyl- and propylparaben (MP, EP, and PP), as well as of their mixture. CNNs with high surface area display superior photocatalytic performance under solar irradiation, offering > 95% degradation efficiency to all parabens, in contrast to the much inferior performance of CNB (< 30%). Several experimental parameters, involving catalyst concentration, initial concentration of parabens, and irradiation type were thoroughly investigated for the degradation of MP over CNNs. Moreover, various scavengers were employed to discriminate the role of different reactive species, revealing that superoxide anion radicals ($\cdot O_2^-$) play a pivotal role in the degradation process, in contrast to hydroxyl radicals (·OH). The present results pave the way towards the facile synthesis of high surface area CNNs with improved textural and electronic characteristics, which can be applied in various environmental applications.

Keywords g-C_3N_4 nanosheets · Solar light irradiation · Photocatalytic activity · Parabens · Radical scavenging experiments

✉ V. Binas
binasbill@iesl.forth.gr

1 Institute of Electronic Structure and Laser (IESL), FORTH, 71110 Heraklion, Greece

2 Industrial, Energy and Environmental Systems Lab (IEESL), School of Production Engineering and Management, Technical University of Crete, 73100 Chania, Greece

3 Department of Chemical Engineering, University of Patras, 26500 Patras, Greece

4 Institute of Chemical Engineering Sciences (ICE-HT), FORTH, 26504 Patras, Greece

5 Department of Physics, University of Crete, 71110 Heraklion, Greece

6 Division of Chemistry, School of Advanced Sciences, VIT Chennai, Chennai 600 025, India

7 Physical Chemistry Laboratory, Chemistry Department, Aristotle University of Thessaloniki, 54124 Thessaloníki, Greece

1 Introduction

Nowadays, the issue of water pollution has caused great concern in the scientific community due to the significant increase of dangerous organic compounds in wastewater. Among the different pollutants, pharmaceuticals and personal care products (PPCPs) are considered widespread contaminants due to their potentially hazardous impact on aquatic life and human health [1, 2].

Parabens, which belong to the category of PPCPs, find widespread usage as preservatives and antimicrobials in cosmetics, pharmaceuticals, processed foods, and various industrial products [3]. They have been classified as endocrine disruptors and are acknowledged as emerging contaminants due to their continuous release in aquatic environments and detection at ng/L to μg/L levels [4], ecotoxicity to various microorganisms [5], and mild estrogenicity [6]. The key reason for their widespread use as preservatives is primarily

attributed to their remarkable effectiveness against fungi and gram-positive bacteria [3]. However, the safety of paraben-containing products remains a subject of substantial debate. Recent concerns have underscored potential risks to water quality, human health, and the ecosystem. Direct exposure to parabens occurs during the use of PPCPs, leading to their detection in human tissues (up to 5103 mg/g) [7] and urine samples (up to 1710 mg/L) [8], among other sources. Several studies have reported the estrogenic and carcinogenic effects of parabens, underscoring the urgent need to eliminate these contaminants from wastewater and other aqueous effluents [3, 9]. Given the documented risks, it is crucial to address and mitigate the presence of parabens to safeguard human health and preserve the integrity of the environment.

In recent years, the need to effectively eliminate paraben preservative products from wastewater has led to the exploration of various advanced oxidation processes [1, 3, 9, 10]. One particularly promising technology is heterogeneous photocatalysis, which offers numerous advantages such as affordability, simplicity, and non-toxicity [1]. This technique has proven to be highly efficient in degrading a wide range of preservative products under ambient temperature and pressure conditions [11]. The photocatalytic reaction involves three primary stages, such as (1) light absorption, (2) separation and transfer of photo-generated electrons (e^-)-holes (h^+), and (3) redox reaction on photocatalyst surface [3, 9]. Despite the many advantages of photocatalysis, its efficiency is still considered relatively low and requires further investigation. Therefore, recent studies have focused on two key areas: developing solar light-responsive photocatalysts and optimizing experimental conditions to enhance the photocatalytic performance and stability of these catalysts [10–19].

Recently, g-C_3N_4 has attracted a great deal of research interest as a photocatalyst, due to its outstanding physicochemical properties, thermal/chemical stability, and suitable band gap with an adequate visible light response [20, 21]. It could be easily synthesized using inexpensive carbon and nitrogen-based precursors [22, 23] and used for organic compound degradation, water splitting, CO_2 reduction, NOx removal, and organic synthesis under visible light [24–31]. Nevertheless, bulk g-C_3N_4 possesses several limitations, including low surface area due to the stacking of layers during polycondensation, insufficient visible light utilization, and rapid recombination of photogenerated electron–hole pairs, leading to low photocatalytic efficiency [32]. To overcome these limitations, several strategies have been employed, such as the construction of heterojunctions, the creation of structural defects, and doping [33–36]. In this direction, the exfoliation process of bulk g-C_3N_4 into thin-layer g-C_3N_4 nanosheets is a low-cost and facile process, leading to a high specific surface area, enhanced physicochemical properties, and increased photocatalytic activity [26, 32, 37, 38].

In the case of the photocatalytic degradation of parabens, several semiconductors have been used [18, 39–41], but only a few studies have been focused on g-C_3N_4. Arvaniti et al. [28] studied the photocatalytic degradation of methylparaben using g-C_3N_4 as a photocatalyst under solar irradiation and reported its complete degradation after 90 min of irradiation at the lowest methylparaben concentration. In addition, Fernandes et al. [42] focused on the photocatalytic degradation of MP, EP, and PP (0.08 mM of initial concentration of each paraben), using the exfoliated g-C_3N_4 (1 g/L) under visible irradiation, revealing complete degradation of each paraben after 20 min of irradiation. Furthermore, Kumar et al. [43] synthesized and used nano-hybrids of magnetic biochar supported g-C_3N_4/$FeVO_4$ for the degradation of methylparaben, via adsorption, photocatalysis, and photo-ozonation. The results showed 98.4% degradation of methylparaben after 90 min of reaction under solar light irradiation.

Inspired by the aforementioned issues, this work aims for the first time at investigating the photocatalytic activity and stability of high surface area CNNs under solar irradiation using MP, EP, and PP as well as their mixture as pollutants. In particular, the present work focused on the comparative study of photocatalytic activity between CNB and CNNs. A complementary characterization analysis, involving BET, XRD, Raman, SEM/TEM, AFM, UV–Vis diffuse reflectance, and Photoluminescence (PL) spectroscopy, was carried out over both CNB and CNNs to gain insight into the effect of thermal exfoliation on the physical and chemical characteristics. The photocatalytic performance of both CNB and CNNs was comparatively assessed for the degradation of MP, EP, and PP as well as their mixture. Several experimental parameters, involving catalyst concentration, initial concentration of parabens, irradiation type as well as the addition of different scavengers were thoroughly investigated. Interestingly, the highly porous CNNs exhibited excellent photocatalytic activity and stability under simulated solar irradiation, in contrast to CNB. The present findings are discussed on the basis of the characterization results in conjunction with the underlying mechanism of parabens degradation over CNNs.

2 Experimental section

2.1 Materials

Methyl-paraben (MP), ethyl-paraben (EP), propyl-paraben (PP), melamine, disodium ethylenediaminetetraacetate dihydrate (EDTA-Na_2), and isopropyl alcohol (IPA) were of analytical grade and purchased from Sigma-Aldrich (Sigma-Aldrich, St. Louis, MO, USA). For the preparation of all solutions and in all experiments, distilled water was used.

2.2 Synthetic procedure of g-C_3N_4

Bulk g-C_3N_4 (CNB) was prepared by thermal polycondensation of melamine and porous g-C_3N_4 nanosheets (CNNs) were obtained via thermal exfoliation of CNB, as thoroughly described in our previous work [37]. In a typical experiment, 50 g of melamine was taken in a covered alumina crucible and calcined at 510 °C for 2 h and 530 °C for 2 h under airflow (heating rate 2 °C/min) in a muffle furnace. The product was a dark yellow solid (named CNB) that was milled and collected for further use. Then, 5 g of CNB was added in an open alumina crucible and calcined at 580 °C for 2 h (heating rate 2 °C/min) in a muffle furnace. The color of the sample was pale yellow (named CNNs) and the volume of the CNNs with the same weight is much larger than that of CNB, demonstrating the high porosity of CNNs.

2.3 Materials characterization

The textural features of both Bulk and CNNs were evaluated by N_2 adsorption–desorption isotherms at − 196 °C (Nova 2200e Quantachrome flow apparatus, Florida, USA). Moreover, the structural features were analyzed through X-ray diffraction (XRD) in a Rigaku diffractometer (model RINT 2000, Tokyo, Japan). For the morphological/surface investigation, Scanning Electron Microscopy (SEM, JEOL JSM-6390LV, JEOL Ltd., Akishima, Tokyo, Japan), as well as Transmission Electron Microscopy (TEM) on a JEM-2100 instrument (JEOL, Tokyo, Japan) was carried out. Atomic force microscopy (AFM) was conducted on a Bruker Dimension Icon under ambient conditions. For the topographic images, silicon nitride ScanAsyst-Air probes (R = 2 nm, k = 0.4 N/m, f = 70 kHz) were used. The samples were dispersed in ethanol and spin-coated (1500 rpm, 1 min) on top of SiO_2/Si. The UV–Vis/Near-IR diffuse reflectance spectra of the materials were received using a Perkin Elmer LAMBDA 950 in the wavelength range of 250–2500 nm with BaSO4, as the reference standard. The optical band gap energies of the samples were determined by plotting the Kubelka–Munk function. Photoluminescence spectra were obtained with a fluorescence spectrophotometer (Agilent Technologies) equipped with a Xenon lamp at an excitation wavelength of 325 nm.

2.4 Photocatalytic experiments

The photocatalytic degradation of single parabens or a mixture of them over the CNB and CNNs was performed on a solar simulator (Mega Lab, model MegCeraX10) equipped with a 300 W xenon lamp and an Air Mass 1.5 Global Filter simulating solar irradiation (> 280 nm). In a typical experiment, 100 mL of the aqueous solution containing 10 mg/L of MP, EP, PP, or their mixture (10 mg/L of initial concentration of each paraben), were loaded in a reaction vessel at ambient temperature under continuous stirring. 50 mg of the as-prepared photocatalyst was added to the reaction solution and this suspension was stirred for 30 min in the dark for an adsorption–desorption equilibrium. At a specified time, samples were collected and filtered by a 0.45 µm diameter glass microfiber Whatman syringe filter. The absorbance of the samples was measured using UV–Vis spectroscopy (Cary 50, Agilent Technologies), and the maximum intensity of the main absorption peak of each paraben was 255 nm. Experiments without catalysts were performed to assess the influence of other processes, such as photolysis, on the degradation of MP, EP, and PP.

Furthermore, the effect of the catalyst concentration (0.1–0.75 g/L), the initial concentration of paraben (0.001–0.02 g/L), and the irradiation type were investigated using CNNs as photocatalyst and MP as a model pollutant. In the case of the experiments under visible irradiation, a filter with a 420 nm cut-off was used. In addition, the reactive species that participated in the photocatalytic process were determined by using various scavengers. Typically, 10 mM isopropyl alcohol (IPA) and disodium ethylenediaminetetraacetate dihydrate (EDTA-Na_2) were used as ·OH and h^+ scavengers, respectively, while a photocatalytic experiment was conducted under a nitrogen atmosphere to quench $\cdot O_2^-$. To investigate the reusability of CNNs, three photocatalytic recycles were carried out. Typically, MP solution containing CNNs was centrifuged and then the precipitate was washed with water, centrifuged, and left to dry overnight. After each cycle, this process was performed to isolate the photocatalyst.

3 Results and discussion

3.1 Structural and morphological alterations between bulk and exfoliated materials

Figure 1a shows the XRD patterns of melamine, CNB, and CNNs. It has been revealed that the starting materials and temperatures can affect condensation, which could be confirmed by the sharp peaks of XRD patterns [26, 38]. In this work, melamine was used as a precursor and in Fig. 1a it is shown that it could finally get the g-C_3N_4 characteristic XRD peaks at 2θ of 13.1° (100) and 27.6° (002). From XRD patterns of as-synthesized samples, the diffraction peak at 27.6° corresponds to the interlayer stacking of the conjugated aromatic systems, and the peak at 13.1° is ascribed to the in-plane structural packing motif [44]. After the exfoliation process, there is a significant reduction in the intensity of the (100) and (002) peaks on CNNs, indicating the successful exfoliation of CNB, resulting in a decrease in the size of the layers, as further discussed below.

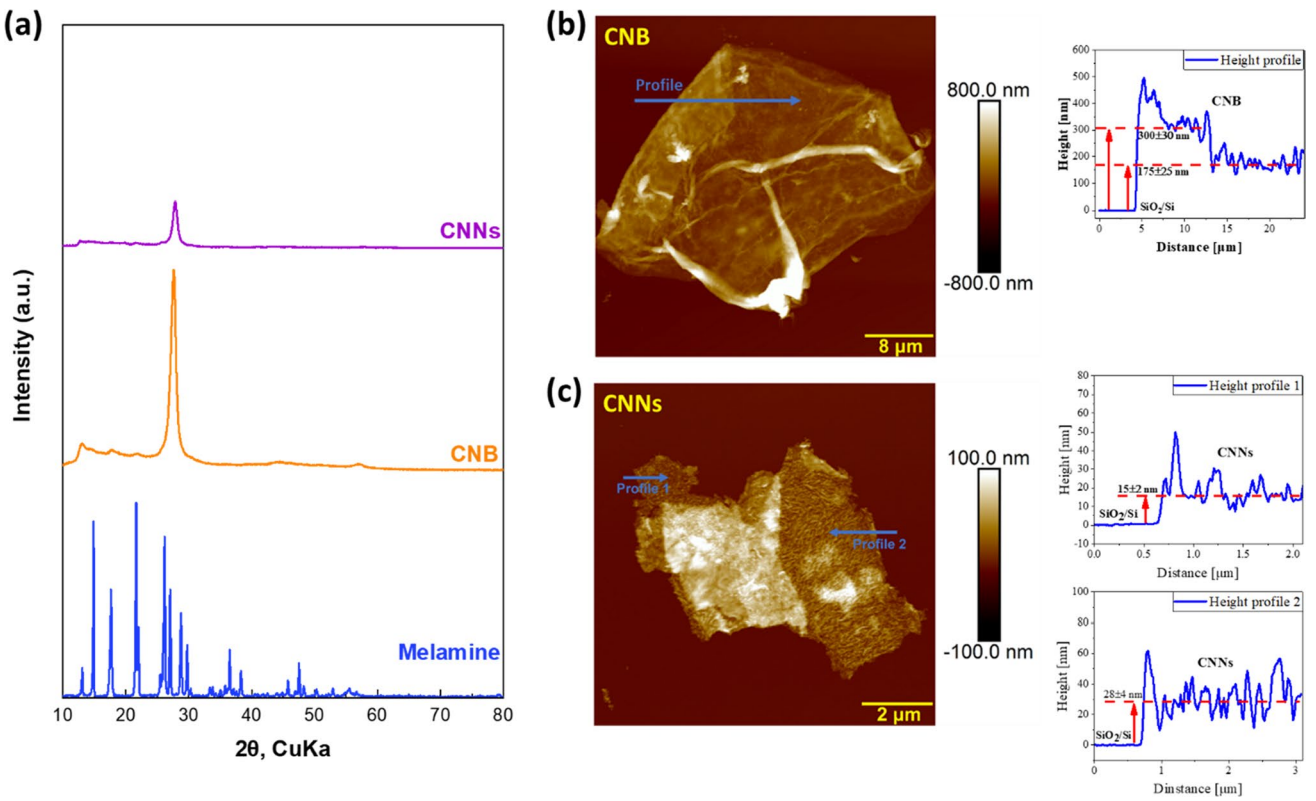

Fig. 1 **a** XRD patterns of melamine, CNB, and CNNs; **b** topography with a respective height profile of CNB. Inset shows a magnified image of its surface. **c** Topography with respective height profiles of CNNs. Inset shows a high-resolution magnified image of its porous surface

The morphology of CNB and CNNs were investigated by SEM and TEM as shown in Figure S1. As depicted in Figure S1(a), CNB is compact and exhibits irregularly stacked large micrometer-sized particles. After the exfoliation process, CNNs exhibit loose agglomerates with abundant pores and thin curved nanosheets (Figure S1(b)). To further investigate the microstructure of the samples, TEM images of both CNB and CNNs are presented in Figure S1(c) and (d), respectively. The CNB agglomeration and stacking are evident again, while CNNs consist of much thinner sheets, confirming the successful exfoliation of the CNB, consistent with the SEM and XRD observations.

To gain insight into the topography and thickness of the materials AFM was in addition employed. Figures 1b and c show CNB and CNNs isolated flakes along with their characteristic topographies and height profiles, respectively. The preparation of CNB resulted in stacked flakes, as seen previously from SEM and TEM images, with a thickness ranging from 175 to 300 nm due to their inhomogeneous agglomeration (Fig. 1b). On the other hand, the exfoliated CNNs produced from the quite violent, thermal exfoliation process, display a nonuniform thickness across the flake, ranging from 15 to 28 nm (Fig. 1c). Diving deeper into the surface of each material (insets of Fig. 1b and c), we can see a distinctive porous nanostructure on the CNNs while CNB is mostly non-porous with high roughness due to layer irregularity. The CNB roughness, at 30 ± 5 nm, is mainly ascribed to the randomly stacked flakes on the investigated area. The thermal exfoliation process significantly reduced the number of sheets and exposed a highly porous surface, resulting in a very high surface area (212 m^2/g), as compared to 10 m^2/g of CNB (Table 1) The roughness of CNNs, at 10 ± 1 nm, is credited to the porous structure while the thickness of the layers has a lesser impact. Taking into consideration the increased roughness in correlation with the thickness, we assume that CNNs vary from 5 to 15 layers whereas CNB fluctuates up to 200 layers (Table 1).

Table 1 Textural/morphological/optical properties of CNB and CNNs samples

Sample	BET analysis		AFM analysis		DRS analysis
	S_{BET} (m^2/g)	Pore volume (cm^3/g)	Thickness (nm)	Roughness (nm)	Band gap (eV)
CNB	10	0.12	200–300	30 ± 5	2.74
CNNs	212	1.07	15–30	10 ± 1	2.91

3.2 Optical properties of bulk and exfoliated materials

The optical properties of the as-prepared samples were determined by UV–visible absorption spectroscopy (UV–Vis DRS). As illustrated in Fig. 2a, the CNB and CNNs samples exhibit an absorption edge in the visible region. However, the absorption edge of the CNNs presents a small blue shift compared to CNB which agrees with the color change. The band gap values of the samples were determined from the Kubelka–Munk function and presented in Table 1 and Fig. 2b, from which it can be observed that the band gap energy (E_g) is increased from 2.74 to 2.91 eV after the exfoliation process [45–47]. As a result, the small blue shift can be ascribed to the quantum confinement effect (QCE) due to the reduction in the thickness and size of the layers of g-C_3N_4 [25, 26, 38, 48].

The band edge potentials of CNB and CNNs were estimated using the following Eqs. (1) and (2)

$$E_{VB} = \chi - E^e + 0.5E_g \quad (1)$$

$$E_{CB} = E_{VB} - E_g \quad (2)$$

where E_{VB} and E_{CB} are potential energy (eV) of the Valance Band (VB) and Conduction Band (CB) respectively; χ is the geometric mean of the electronegativity of the constituent atoms of a semiconductor (calculated to be 4.73 eV for g-C_3N_4); E^e is the energy of free electrons in a standard hydrogen electrode (~4.5 eV vs NHE) [49, 50]; Eg is the experimentally determined band gap energy of the sample. As we can see in Fig. 2c, the E_{CB} of both CNB and CNNs are about − 1.14 and − 1.23 eV, respectively, whereas the E_{VB} values are estimated to be 1.60 and 1.69 eV, respectively, in accordance with those reported in the literature [49–52].

To assess the emission and exciton recombination dynamics of CNB and CNNs, PL spectra were acquired at room temperature at a 325 nm excitation wavelength. As is common from reducing the thickness of 2D semiconductors [53, 54], the PL intensity of CNNs is higher than the bulk counterpart, as shown in Fig. 2d. This effect is due to the higher crystallinity and more condensed packing of the exfoliated samples, which reduces the number of structural defects [38]. After Gaussian fitting of the spectra, we can discern three emission peaks from the recombination of electron–hole pairs (Fig. 2e, f). The bandgap states of g-C_3N_4 consist of a sp^3 C–N σ band, sp^2 C–N π band, and the lone pair (LP) state of the bridge nitride atom. P1, P2, and P3 originate from the pathways of transitions: π^*–π, σ^*–LP, and π^*–LP respectively [55]. The P1 peak is found at 434 nm and 430 nm for CNB and CNNs respectively, denoting the band-to-band transition. The blue shift

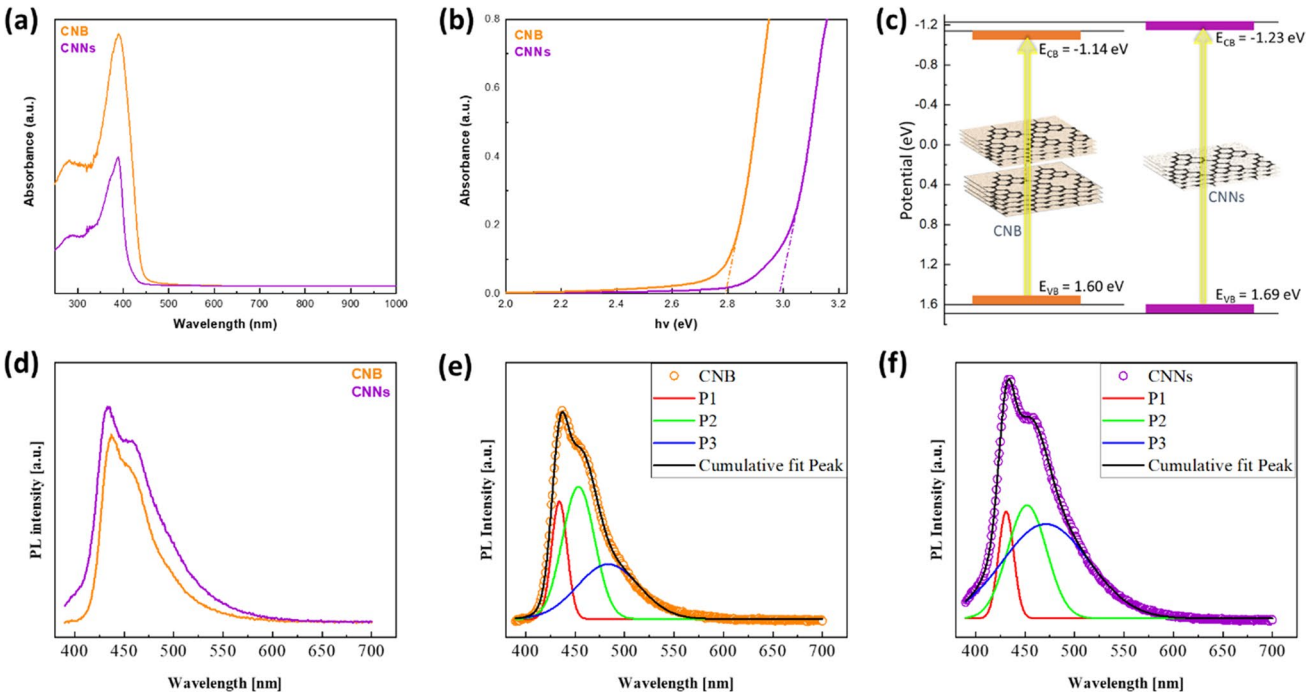

Fig. 2 **a** UV–Vis diffuse reflectance spectra of CNB and CNNs; **b** band gaps obtained from Kubelka–Munk function of CNB and CNNs; **c** schematic illustration of morphology evolution of g-C_3N_4 after exfoliation, along with their corresponding band structure; **d** PL spectra of CNB and CNNs at room temperature at a 325 nm excitation wavelength; Gaussian fitting of the **e** CNB and **f** CNNs P1, P2, and P3 exciton peaks

of the P1 emission peak is corroborated here also and is ascribed to QCE induced by thin/small nanosheets and the gradual transitioning from an indirect to a direct band gap. Since the majority of the exfoliated flakes are thicker than a monolayer, we still have the indirect regime, hence the appearance of the P2 exciton peak. P2 peak is situated at 452 nm for both materials, which is attributed to indirect band-to-band transitions. P3 broad peak is found at 483 nm and 470 nm for CNB and CNNs respectively and is ascribed to the recombination of electron–hole pairs due to structural defects still present in the materials. CNNs P3 peak showcases an increase in the density of defects even after the exfoliation process. To account for this behavior we should fathom the role of the surface and bulk defects. Generally, the defect density on the surface is considered higher than in the bulk [56]. However, by taking into consideration the penetration depth of the excitation wavelength (325 nm), PL cannot probe the whole range of bulk defects [57]. Hence, the defect density of CNNs compared to CNB appears to be higher.

3.3 Photocatalytic degradation

3.3.1 Evaluation of catalyst activity

The photocatalytic performance of CNB and CNNs toward degradation of methyl-, ethyl-, and propyl-parabens, as well as of their mixtures (denoted as MP, EP, PP, and Mixed parabens respectively) under solar irradiation, was investigated. Firstly, experiments were carried out without the use of a catalyst, and no significant change in the concentration of MP, EP, and PP was observed (blank test). Figure 3a illustrates the variations of concentration of three different parabens (MP, EP, PP, and Mixed parabens) versus degradation time in the presence of catalysts under solar irradiation. To achieve an adsorption–desorption equilibrium, the suspension was stirred in the dark for 30 min prior to irradiating

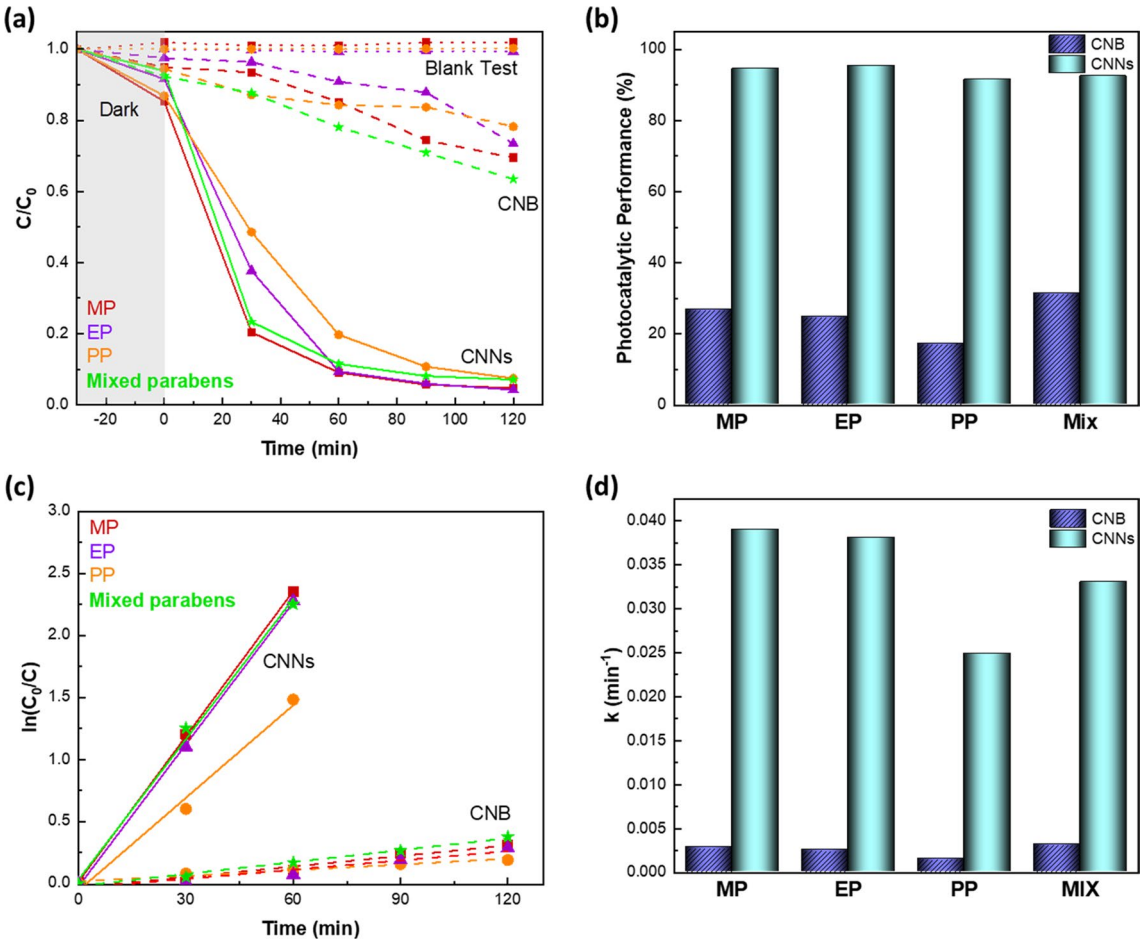

Fig. 3 **a** Photocatalytic degradation of MP, EP, and PP over CNB and CNNs, **b** the comparison of the photocatalytic performance of CNB and CNNs for the removal of MP, EP, and PP, **c** the linear plots of $\ln(C_0/C)$ versus degradation time, **d** degradation rate constant k values of CNB and CNNs (initial conditions: 0.01 g/L parabens, 0.5 g/L photocatalyst, solar light irradiation)

each sample. As shown in Fig. 3a, this step caused only a minor reduction in pollutant concentration (< 15%). Upon initiating irradiation, a significant decrease in concentration was observed for CNNs. Specifically, the photocatalytic performance of CNNs was found to be 94.5%, 95.4%, 91.4%, and 92.4% for the degradation of MP, EP, PP, and mixed parabens, respectively, after 120 min of solar light irradiation. In contrast, CNB exhibits much lower photocatalytic efficiency of 26.8%, 24.7%, 17.2%, and 31.3% for the removal of MP, EP, PP, and Mixed parabens, respectively. These results, summarized in Table S1 and comparatively depicted in Fig. 3b, clearly demonstrate the superior photocatalytic activity of CNNs as compared to CNB for the degradation of investigated parabens. Moreover, a literature comparison with relevant studies, is included in Table S2. It is evident, that the as-synthesized CNNs exhibit excellent photocatalytic performance for the simultaneous removal of MP, EP, PP, and mixed parabens under solar light irradiation. It should be also stressed that the as-prepared samples are characterized by a facile preparation method and simple composition, in contrast to the most studies employing multifunctional composites of complex composition (Table S2).

The photocatalytic degradation follows pseudo-first-order kinetics, and the linear plots of $\ln(C_0/C)$ versus irradiation time for CNB and CNNs are shown in Fig. 6c. The degradation rate constant k values are comparatively shown in Fig. 6d and summarized in Table S2. The superiority of CNNs is again obvious, revealing the pronounced effect of the exfoliation process towards obtaining nanostructured g-C_3N_4 with high surface area, which in turn is reflected in the photocatalytic performance. In particular, the increase in the surface area can lead to decreased recombination rate of photogenerated charges and thus enhanced photocatalytic activity.

3.3.2 Effect of catalyst concentration

The impact of increasing catalyst concentration in the range of 0.1–0.75 g/L on MP degradation is shown in Fig. 4a. As we can see, the highest photocatalytic performance of CNNs was found to be 0.5 g/L after 120 min of solar light irradiation (94.5%), followed by 0.75 g/L (91.5%), 0.25 g/L (89.8%) and 0.1 g/L (86.2%), as shown in Table S3. Taking into account that the photocatalytic degradation under specific reaction conditions depends on the population and reactivity of photocatalytic sites in conjunction with reactants concentration, the present findings reveal an optimum catalyst concentration of 0.5 g/L. A similar trend has been reported in various studies, where no further increase in degradation rate was obtained after a threshold loading, ascribed mainly to scattering and screening phenomena which could result in the non-uniform light intensity distribution [58].

3.3.3 Effect of initial concentration

Figure 4b illustrates the influence of the initial MP concentration (0.001–0.02 g/L) on its degradation using CNNs as a photocatalyst. The reaction rate constant k of MP degradation and photodegradation efficiency of CNNs did not change significantly after 120 min of photocatalytic reaction at all concentration levels tested for MP. The following order, both in terms of reaction rate constant k and photodegradation efficiency, was obtained: 0.01 g/L > 0.005 g/L > 0.001 g/L > 0.02 g/L, as presented in Table S3. Although CNNs achieved the highest degradation of MP at 0.01 g/L (94.5%), these results revealed that CNNs could successfully degrade MP over a wide range of its concentrations.

3.3.4 Effect of irradiation type

Apart from the effect of the catalyst concentration and the initial concentration of parabens, the effect of the irradiation type was assessed. Especially, the photocatalytic degradation of 0.01 g/L MP with 0.5 g/L CNNs under solar and visible irradiation is illustrated in Fig. 4c. The photocatalytic activity of CNNs is 94.8% and 78.6% for the degradation of MP under solar and visible irradiation. To investigate that MP degradation is owing to interactions between photons and the surface of the catalyst, an additional experiment was carried out without a catalyst, and the results showed almost zero removal after 120 min of solar irradiation. The reaction rate constant k under solar irradiation is ca. 3 times greater than that of visible, implying the key role of irradiation type (Table S3).

3.3.5 CNNs reusability and stability

The stability and reusability of a photocatalyst play a significant role in its practical application. In view of this point, three photocatalytic cycles were conducted to degrade MP over CNNs under solar light by collecting and reusing the photocatalyst. The photocatalytic stability experiments of CNNs are shown in Fig. 4d and no significant loss of its activity has been detected (> 90% of MP degradation) after three cycles, indicating its high stability.

The excellent long-term stability of the CNNs is further confirmed by the XRD pattern after repeated reaction cycles (Figure S3). The crystal structure of fresh and after three reaction cycles CNNs indicate their excellent phase stability.

3.3.6 Mechanism of parabens degradation over CNNs

It has been well established that the photocatalytic performance is strongly related to the textural/structural as well as the redox/electronic properties of the employed material. The former could be accounted for the abundance and

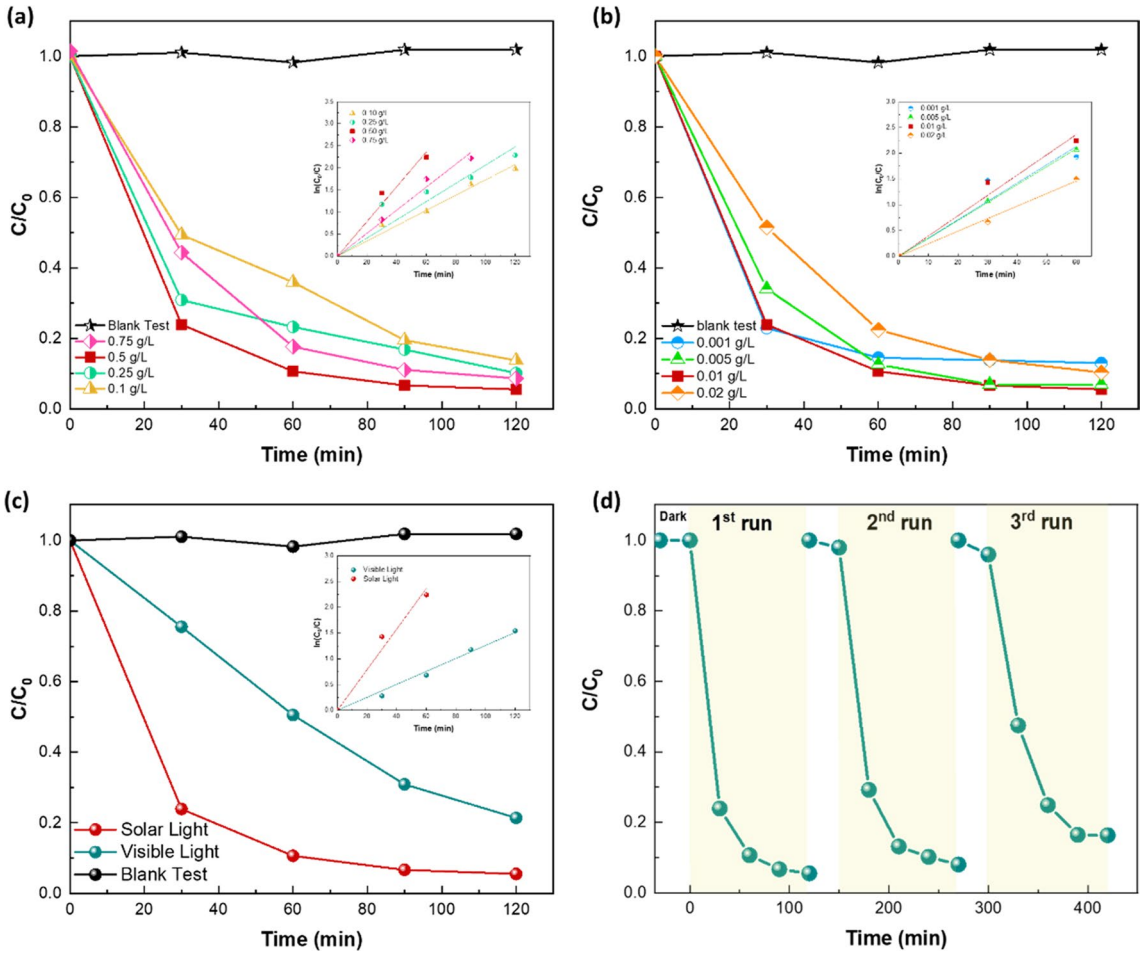

Fig. 4 **a** Effect of the catalyst concentration (initial conditions: 0.01 g/L MP, solar light irradiation); **b** effect of initial concentration of MP on the photocatalytic activity of CNNs (initial conditions: 0.5 g/L CNNs, solar light irradiation); **c** photocatalytic degradation of MP under visible or solar irradiation with CNNs (initial conditions: 0.5 g/L CNNs, 0.01 g/L MP); **d** stability and reusability of CNNs for the degradation of MP (initial conditions: 0.5 g/L CNNs, 0.01 g/L MP, solar light irradiation)

distribution of active sites whereas the latter could be related to the separation and recombination of photogenerated electron–hole pairs, linked with interfacial charge transfer phenomena. Under these perspectives, the superior textural characteristics of CNNs (BET surface area of 212 m^2/g) could provide more active sites for the redox reactions, thereby rendering the photocatalytic process more efficient. Apart from the textural characteristics, the semiconductor photoexcitation is expected to be notably influenced by the photo-absorption ability and the band gap of the photocatalyst. In the present work, the band gap obtained for CNB and CNNs was 2.74 and 2.91 eV, respectively (Table 1). The increase in the band gap of g-C_3N_4 induced by the thermal exfoliation process can be ascribed to the quantum confinement effect (QCE). According to this, the bandgap can increase due to the opposite shift between the valence and conduction band edges. Therefore, CNNs could provide more powerful photogenerated electron–hole pairs, decreasing the recombination rate of the photogenerated electrons and holes. Additionally, the migration distance of charges from the bulk to the surface was significantly decreased after the delamination, thus reducing the probability of recombination during migration.

To further gain insight into the underlying mechanism of photocatalytic degradation of parabens on CNNs, various scavengers were employed. Isopropyl alcohol (IPA) and disodium ethylenediaminetetraacetate dihydrate (EDTA-Na_2) were used as ·OH and h^+ scavengers while a photocatalytic test was carried out under a nitrogen atmosphere to remove $\cdot O_2^-$. As presented in Fig. 5, the test without scavenger shows that the photocatalytic degradation of MP over CNNs was 93.3% after 90 min solar irradiation. When IPA was added, only a small decrease in photocatalytic degradation was observed, revealing the negligible role of ·OH radical. However, the photocatalytic activity of CNNs was significantly decreased by degassing with

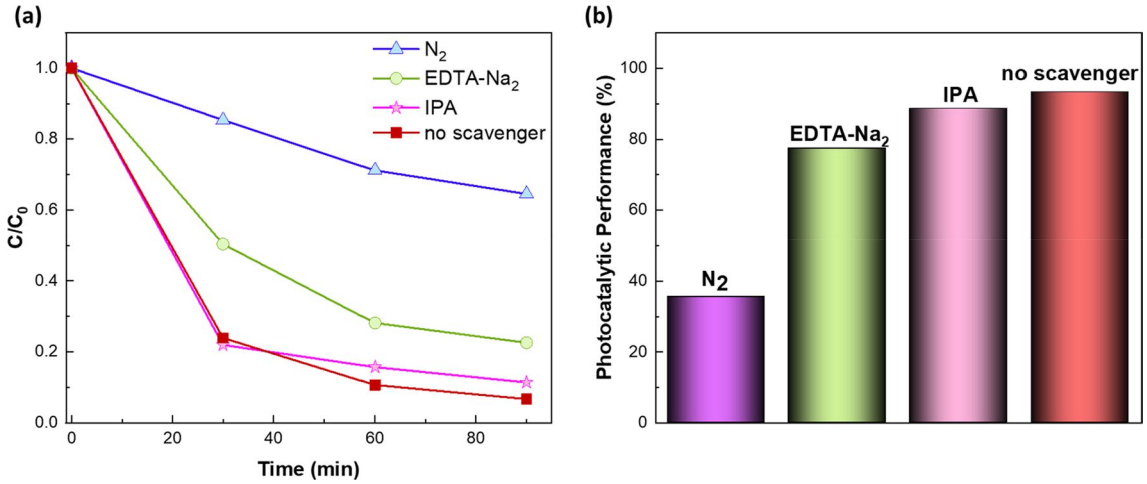

Fig. 5 **a** Photocatalytic degradation of MP over CNNs and **b** the photocatalytic performance of CNNs, in the presence of various scavengers (initial conditions: 0.5 g/L CNNs, 0.01 g/L MP, solar light irradiation)

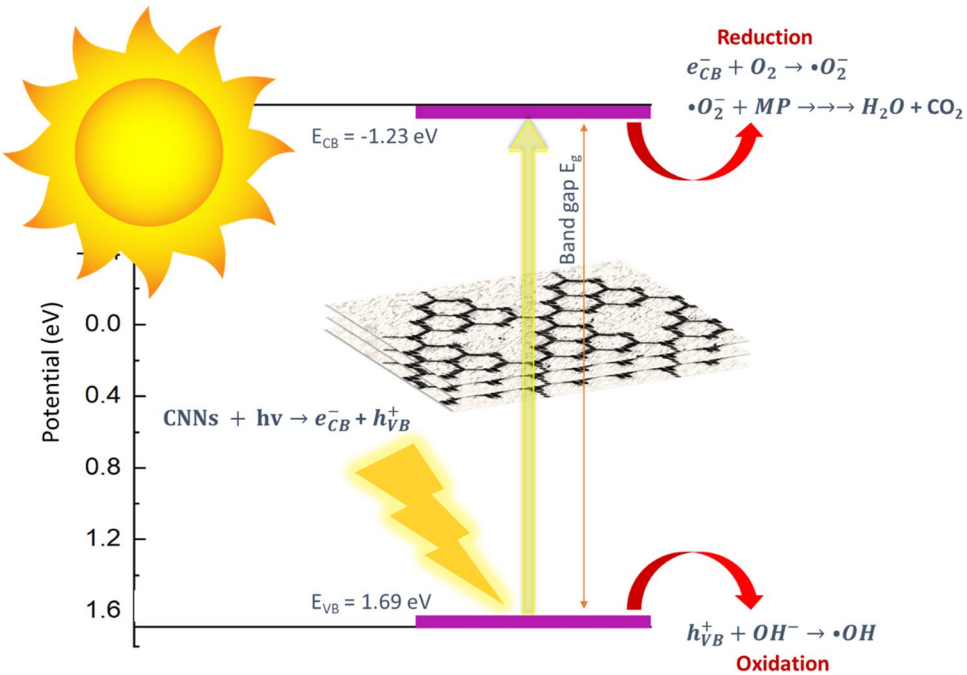

Fig. 6 Schematic diagrams of the photocatalytic mechanism of CNNs under solar light irradiation

N_2, whereas an intermediate effect was obtained by the addition of EDTA-Na_2. More specifically, the following order was obtained using various scavengers: no scavenger (93.3%) > IPA (88.6%) > EDTA-Na_2 (77.4%) > N_2 (35.5%) for 90 min solar irradiation. Moreover, the reaction rate constant k was calculated in all cases and exhibited the same trend as the photodegradation efficiency of CNNs, as shown in Table S4. On the basis of these results, it could be argued that superoxide radicals ($\cdot O_2^-$) play a vital role in the photodegradation reaction, followed by holes (h^+), whereas the contribution of hydroxyl radical (·OH) could be considered minor.

In light of the above considerations, the photocatalytic degradation mechanism of CNNs under solar irradiation is schematically illustrated in Fig. 6. Specifically, the energy level at the bottom of the CB is the photoelectrons reduction potential while the energy level at the top VB determines the oxidizing ability of generated holes (Fig. 2c). These values reflect the ability of the system to promote reduction and oxidation processes, respectively. Hence, the photogenerated electrons can reduce the adsorbed molecular oxygen, producing superoxide radicals and the generated holes can react with water molecules giving hydroxyl radicals. Consequently, according to the trapping

experiments of active species, the photocatalytic degradation of MP over CNNs can be attributed to $\cdot O_2^-$ radicals and h^+ with strong oxidative potential, which can effectively degrade the organic pollutant to CO_2 and H_2O.

4 Conclusions

In the present work, high surface area g-C_3N_4 nanosheets (CNNs) were successfully synthesized by thermal exfoliation of bulk g-C_3N_4 (CNB). A comparative photocatalytic study between CNB and CNNs was carried out for the degradation of methyl-, ethyl-, and propyl-parabens, as well as their mixture A thorough physicochemical characterization of both CNB and CNNs materials using various techniques, clearly discloses the superiority of CNNs in terms of textural (surface area of 212 m^2/g) and optical properties (wide band gap of 2.91 eV). This in turn is reflected in its excellent photocatalytic efficiency under solar light irradiation of CNNs, offering > 95% degradation to all types of parabens, as compared to much inferior performance (< 30%) of CNB. In addition, CNNs attained high photocatalytic and structural stability after 3 consecutive photocatalytic cycles. Radical scavenging experiments revealed that superoxide radicals ($\cdot O_2^-$), followed by holes (h^+) play an essential role in the degradation process, in contrast to hydroxyl radicals (·OH).

Supplementary Information The online version contains supplementary material available at https://doi.org/10.1007/s00339-023-07032-y.

Acknowledgements The present work was financed by the LIFE VISIONS project (LIFE19 ENV/GR/000100) with the contribution of the LIFE Programme of the European Union. This work reflects only the authors' view and CINEA is not responsible for any use that may be made of the information it contains. Furthermore, part of this work was co-financed by Greece and the European Union (European Social Fund-ESF) through the Operational Programme "Human Resources Development, Education and Lifelong Learning" in the context of the Act "Enhancing Human Resources Research Potential by undertaking a Doctoral Research" Sub-action 2: IKY Scholarship Programme for Ph.D. candidates in the Greek Universities.

Author contributions Conceptualization SS and VB; methodology, investigation and data curation MZ, SS, MD, PS, CG, GK and GP; validation SS and VB; original draft preparation SS, VB; draft review and editing MK and VB; supervision, VB; project administration and funding acquisition VB. All authors have read and agreed to the published version of the manuscript.

Funding Open access funding provided by HEAL-Link Greece.

Data availability Data can be available upon reasonable request.

Declarations

Conflict of interest The authors declare that they have no known competing financial interests or personal relationships that could have appeared to influence the work reported in this paper.

References

1. T.O. Ajiboye, O.A. Oyewo, D.C. Onwudiwe, Simultaneous removal of organics and heavy metals from industrial wastewater: a review. Chemosphere **262**, 128379 (2021). https://doi.org/10.1016/j.chemosphere.2020.128379
2. G. Xia, Y. Zheng, Z. Sun, S. Xia, Z. Ni, J. Yao, Fabrication of ZnAl-LDH mixed metal-oxide composites for photocatalytic degradation of 4-chlorophenol. Environ. Sci. Pollut. Res. **29**(26), 39441–39450 (2022). https://doi.org/10.1007/s11356-022-18989-3
3. V.-H. Nguyen et al., The degradation of paraben preservatives: recent progress and sustainable approaches toward photocatalysis. Chemosphere **276**, 130163 (2021). https://doi.org/10.1016/j.chemosphere.2021.130163
4. Y. Gao, Y. Ji, G. Li, T. An, Theoretical investigation on the kinetics and mechanisms of hydroxyl radical-induced transformation of parabens and its consequences for toxicity: Influence of alkyl-chain length. Water Res. **91**, 77–85 (2016). https://doi.org/10.1016/j.watres.2015.12.056
5. M. Gmurek, M. Bizukojć, J. Mosinger, S. Ledakowicz, Application of photoactive electrospun nanofiber materials with immobilized meso-tetraphenylporphyrin for parabens photodegradation. Catal. Today **240**(PA), 160–167 (2015). https://doi.org/10.1016/j.cattod.2014.06.015
6. C. Papadopoulos, Z. Frontistis, M. Antonopoulou, D. Venieri, I. Konstantinou, D. Mantzavinos, Sonochemical degradation of ethyl paraben in environmental samples: statistically important parameters determining kinetics, by-products and pathways. Ultrason. Sonochem. **31**, 62–70 (2016). https://doi.org/10.1016/j.ultsonch.2015.12.002
7. L. Barr, G. Metaxas, C.A.J. Harbach, L.A. Savoy, P.D. Darbre, Measurement of paraben concentrations in human breast tissue at serial locations across the breast from axilla to sternum. J. Appl. Toxicol. **32**(3), 219–232 (2012). https://doi.org/10.1002/jat.1786
8. E.P. Hines, P. Mendola, O.S. von Ehrenstein, X. Ye, A.M. Calafat, S.E. Fenton, Concentrations of environmental phenols and parabens in milk, urine and serum of lactating North Carolina women. Reprod. Toxicol. **54**, 120–128 (2015). https://doi.org/10.1016/j.reprotox.2014.11.006
9. T.O. Ajiboye, O.A. Oyewo, D.C. Onwudiwe, Photocatalytic removal of parabens and halogenated products in wastewater: a review. Environ. Chem. Lett. **19**(5), 3789–3819 (2021). https://doi.org/10.1007/s10311-021-01263-2

10. C. Ding et al., Efficient photocatalysis of tetracycline hydrochloride (TC-HCl) from pharmaceutical wastewater using AgCl/ZnO/g-C_3N_4 composite under visible light: Process and mechanisms. J. Environ. Sci. (China) **126**, 249–262 (2023). https://doi.org/10.1016/j.jes.2022.02.032
11. Y. Liang et al., Benzene decomposition by non-thermal plasma: a detailed mechanism study by synchrotron radiation photoionization mass spectrometry and theoretical calculations. J. Hazard. Mater. **420**(April), 126584 (2021). https://doi.org/10.1016/j.jhazmat.2021.126584
12. Z. Ya et al., An ultra-porous g-C_3N_4 micro-tube coupled with MXene ($Ti_3C_2T_X$) nanosheets for efficient degradation of organics under natural sunlight. J. Environ. Sci. **137**, 258–270 (2022). https://doi.org/10.1016/j.jes.2022.10.049
13. Z. Feng et al., In situ preparation of g-C_3N_4/$Bi_4O_5I_2$ complex and its elevated photoactivity in Methyl Orange degradation under visible light. J. Environ. Sci. (China) **87**(1972), 149–162 (2020). https://doi.org/10.1016/j.jes.2019.05.032
14. H. Yu, J. Zhu, R. Qiao, N. Zhao, M. Zhao, L. Kong, Facile preparation and controllable absorption of a composite based on PMo_{12}/Ag nanoparticles: photodegradation activity and mechanism. ChemistrySelect (2022). https://doi.org/10.1002/slct.202103668
15. S. Kotzamanidi, Z. Frontistis, V. Binas, G. Kiriakidis, D. Mantzavinos, Solar photocatalytic degradation of propyl paraben in Al-doped TiO_2 suspensions. Catal. Today **313**(December 2017), 148–154 (2018). https://doi.org/10.1016/j.cattod.2017.12.006
16. P. Xu, C. Ding, Z. Li, R. Yu, H. Cui, S. Gao, Photocatalytic degradation of air pollutant by modified nano titanium oxide (TiO_2)in a fluidized bed photoreactor: optimizing and kinetic modeling. Chemosphere (2023). https://doi.org/10.1016/j.chemosphere.2023.137995
17. M. Ahmad et al., Enhanced photocatalytic degradation of RhB dye from aqueous solution by biogenic catalyst Ag@ZnO. J. Alloys Compd. **895**, 162636 (2022). https://doi.org/10.1016/j.jallcom.2021.162636
18. Z. Frontistis, M. Antonopoulou, D. Venieri, S. Dailianis, I. Konstantinou, D. Mantzavinos, Solar photocatalytic decomposition of ethyl paraben in zinc oxide suspensions. Catal. Today **280**, 139–148 (2017). https://doi.org/10.1016/j.cattod.2016.06.008
19. M. Moschogiannaki, Z. Frontistis, G. Kiriakidis, D. Mantzavinos, V. Binas, Porous $Co_xNi_{1-x}TiO_3$ nanorods for solar photocatalytic degradation of ethyl paraben. J. Mater. **6**(4), 788–799 (2020). https://doi.org/10.1016/j.jmat.2020.05.006
20. M. Ismael, A review on graphitic carbon nitride (g-C_3N_4) based nanocomposites: synthesis, categories, and their application in photocatalysis. J. Alloys Compd. **846**, 156446 (2020). https://doi.org/10.1016/j.jallcom.2020.156446
21. L. Zhou et al., Recent advances in non-metal modification of graphitic carbon nitride for photocatalysis: a historic review. Catal. Sci. Technol. **6**(19), 7002–7023 (2016). https://doi.org/10.1039/C6CY01195K
22. X. Wang, S. Blechert, M. Antonietti, Polymeric graphitic carbon nitride for heterogeneous photocatalysis. ACS Catal. **2**(8), 1596–1606 (2012). https://doi.org/10.1021/cs300240x
23. Z. Zhao et al., Synthesis of graphitic carbon nitride from different precursors by fractional thermal polymerization method and their visible light induced photocatalytic activities. J. Alloys Compd. **735**, 1297–1305 (2018). https://doi.org/10.1016/j.jallcom.2017.11.033
24. M. Batvandi, A. Haghighatzadeh, B. Mazinani, J. Dutta, Visible-light-driven photocatalysis with Z-scheme Ag_3PO_4@N-GQDs@g-C_3N_4 nano/hetero-junctions. Appl. Phys. A Mater. Sci. Process. **128**(10), 1–18 (2022). https://doi.org/10.1007/s00339-022-06005-x
25. Q. Liang, Z. Li, Z.-H. Huang, F. Kang, Q.-H. Yang, Holey graphitic carbon nitride nanosheets with carbon vacancies for highly improved photocatalytic hydrogen production. Adv. Funct. Mater. **25**(44), 6885–6892 (2015). https://doi.org/10.1002/adfm.201503221
26. X. Wu, J. Cheng, X. Li, Y. Li, K. Lv, Enhanced visible photocatalytic oxidation of NO by repeated calcination of g-C_3N_4. Appl. Surf. Sci. **465**(June 2018), 1037–1046 (2019). https://doi.org/10.1016/j.apsusc.2018.09.165
27. X. Ye, Y. Cui, X. Wang, Ferrocene-modified carbon nitride for direct oxidation of benzene to phenol with visible light. ChemSusChem **7**(3), 738–742 (2014). https://doi.org/10.1002/cssc.201301128
28. O.S. Arvaniti, A. Petala, A.A. Zalaora, D. Mantzavinos, Z. Frontistis, Solar light-induced photocatalytic degradation of methylparaben by g-C_3N_4 in different water matrices. J. Chem. Technol. Biotechnol. **95**(11), 2811–2821 (2020). https://doi.org/10.1002/jctb.6564
29. J. Fu, B. Zhu, C. Jiang, B. Cheng, W. You, J. Yu, Hierarchical porous O-doped g-C_3N_4 with enhanced photocatalytic CO_2 reduction activity. Small **13**(15), 1603938 (2017). https://doi.org/10.1002/smll.201603938
30. G. Ahilandeswari, D. Arivuoli, Investigation of $Ce_2(WO_4)_3$/g-C_3N_4 nanocomposite for degradation of industrial pollutants through sunlight-driven photocatalysis. Appl. Phys. A Mater. Sci. Process. **128**(8), 1–16 (2022). https://doi.org/10.1007/s00339-022-05846-w
31. D.F. Li, K. Yang, X. Qin Wang, Y.L. Ma, G.F. Huang, W.Q. Huang, Enhancement of photocatalytic activity of combustion-synthesized CeO_2/C_3N_4 nanoparticles. Appl. Phys. A Mater. Sci. Process. **120**(3), 1205–1209 (2015). https://doi.org/10.1007/s00339-015-9305-y
32. P. Niu, L. Zhang, G. Liu, H.-M. Cheng, Graphene-like carbon nitride nanosheets for improved photocatalytic activities. Adv. Funct. Mater. **22**(22), 4763–4770 (2012). https://doi.org/10.1002/adfm.201200922
33. S. Hu et al., Enhanced visible light photocatalytic performance of g-C_3N_4 photocatalysts co-doped with iron and phosphorus. Appl. Surf. Sci. **311**, 164–171 (2014). https://doi.org/10.1016/j.apsusc.2014.05.036
34. J. Li et al., Synthesis of MoS_2/g-C_3N_4 nanosheets as 2D heterojunction photocatalysts with enhanced visible light activity. Appl. Surf. Sci. **364**, 694–702 (2016). https://doi.org/10.1016/j.apsusc.2015.12.236
35. J. Ding et al., Nitrogen vacancy engineered graphitic C_3N_4-based polymers for photocatalytic oxidation of aromatic alcohols to aldehydes. Appl. Catal. B Environ. **221**(August 2017), 626–634 (2018). https://doi.org/10.1016/j.apcatb.2017.09.048
36. V. Faka et al., Solar light induced photocatalytic degradation of sulfamethoxazole by $ZnWO_4$/CNNs nanocomposites. J. Photochem. Photobiol. A Chem. **432**(June), 114108 (2022). https://doi.org/10.1016/j.jphotochem.2022.114108
37. S. Stefa et al., Highly porous thin-layer g-C_3N_4 nanosheets with enhanced adsorption capacity. ACS Appl. Nano Mater. **6**(3), 1732–1743 (2023). https://doi.org/10.1021/acsanm.2c04632
38. F. Dong, Y. Li, Z. Wang, W.-K. Ho, Enhanced visible light photocatalytic activity and oxidation ability of porous graphene-like g-C_3N_4 nanosheets via thermal exfoliation. Appl. Surf. Sci. **358**, 393–403 (2015). https://doi.org/10.1016/j.apsusc.2015.04.034
39. X. Xiao et al., Rapid microwave synthesis of I-doped $Bi_4O_5Br_2$ with significantly enhanced visible-light photocatalysis for degradation of multiple parabens. Appl. Catal. B Environ. **218**, 398–408 (2017). https://doi.org/10.1016/j.apcatb.2017.06.074
40. Z. Frontistis et al., Boron-doped diamond electrooxidation of ethyl paraben: the effect of electrolyte on by-products distribution and

mechanisms. J. Environ. Manag. **195**, 148–156 (2017). https://doi.org/10.1016/j.jenvman.2016.06.044
41. Z. Frontistis et al., Photodegradation of ethyl paraben using simulated solar radiation and Ag_3PO_4 photocatalyst. J. Hazard. Mater. **323**, 478–488 (2017). https://doi.org/10.1016/j.jhazmat.2016.04.017
42. R.A. Fernandes, M.J. Sampaio, G. Dražić, J.L. Faria, C.G. Silva, Efficient removal of parabens from real water matrices by a metal-free carbon nitride photocatalyst. Sci. Total. Environ. (2020). https://doi.org/10.1016/j.scitotenv.2019.135346
43. A. Kumar et al., Sustainable nano-hybrids of magnetic biochar supported g-C_3N_4/$FeVO_4$ for solar powered degradation of noxious pollutants—synergism of adsorption, photocatalysis & photo-ozonation. J. Clean. Prod. **165**, 431–451 (2017). https://doi.org/10.1016/j.jclepro.2017.07.117
44. N. Meng, J. Ren, Y. Liu, Y. Huang, T. Petit, B. Zhang, Engineering oxygen-containing and amino groups into two-dimensional atomically-thin porous polymeric carbon nitrogen for enhanced photocatalytic hydrogen production. Energy Environ. Sci. **11**(3), 566–571 (2018). https://doi.org/10.1039/C7EE03592F
45. M. Saleem et al., DFT and experimental investigations on $CdTe_{1-x}Se_x$ for thermoelectric and optoelectronic applications. J. Alloys Compd. **921**, 1–9 (2022). https://doi.org/10.1016/j.jallcom.2022.166175
46. T. Zeeshan et al., A comparative computational and experimental study of Al–ZrO_2 thin films for optoelectronic applications. Solid State Commun. **358**(November), 115006 (2022). https://doi.org/10.1016/j.ssc.2022.115006
47. N. Ullah et al., Effect of cobalt doping on the structural, optical and antibacterial properties of α-MnO_2 nanorods. Appl. Phys. A Mater. Sci. Process. **127**(10), 1–7 (2021). https://doi.org/10.1007/s00339-021-04926-7
48. Y. Li et al., Tuning and thermal exfoliation graphene-like carbon nitride nanosheets for superior photocatalytic activity. Ceram. Int. **42**(16), 18521–18528 (2016). https://doi.org/10.1016/j.ceramint.2016.08.190
49. S. Panneri et al., Photoregenerable, bifunctional granules of carbon-doped g-C_3N_4 as adsorptive photocatalyst for the efficient removal of tetracycline antibiotic. ACS Sustain. Chem. Eng. **5**(2), 1610–1618 (2017). https://doi.org/10.1021/acssuschemeng.6b02383
50. J.H. Thurston, N.M. Hunter, K.A. Cornell, Preparation and characterization of photoactive antimicrobial graphitic carbon nitride (g-C_3N_4) films. RSC Adv. **6**(48), 42240–42248 (2016). https://doi.org/10.1039/c6ra05613j
51. W. Zhang et al., Photocatalytic improvement of Mn-adsorbed g-C_3N_4. Appl. Catal. B Environ. **206**(November), 271–281 (2017). https://doi.org/10.1016/j.apcatb.2017.01.034
52. T. Yan et al., Facile fabrication of heterostructured g-C_3N_4/Bi_2MoO_6 microspheres with highly efficient activity under visible light irradiation. Dalt. Trans. **44**(4), 1601–1611 (2015). https://doi.org/10.1039/C4DT02127D
53. K.F. Mak, C. Lee, J. Hone, J. Shan, T.F. Heinz, Atomically thin MoS_2: a new direct-gap semiconductor. Phys. Rev. Lett. **105**(13), 136805 (2010). https://doi.org/10.1103/PhysRevLett.105.136805
54. A. Splendiani et al., Emerging photoluminescence in monolayer MoS_2. Nano Lett. **10**(4), 1271–1275 (2010). https://doi.org/10.1021/nl903868w
55. Y. Yuan et al., High-yield synthesis and optical properties of g-C_3N_4. Nanoscale **7**(29), 12343–12350 (2015). https://doi.org/10.1039/c5nr02905h
56. D. Ruan, S. Kim, M. Fujitsuka, T. Majima, Defects rich g-C_3N_4 with mesoporous structure for efficient photocatalytic H_2 production under visible light irradiation. Appl. Catal. B Environ. **238**, 638–646 (2018). https://doi.org/10.1016/j.apcatb.2018.07.028
57. C.A. Aggelopoulos, M. Dimitropoulos, A. Govatsi, L. Sygellou, C.D. Tsakiroglou, S.N. Yannopoulos, Influence of the surface-to-bulk defects ratio of ZnO and TiO_2 on their UV-mediated photocatalytic activity. Appl. Catal. B Environ. **205**, 292–301 (2017). https://doi.org/10.1016/j.apcatb.2016.12.023
58. T. Velegraki, E. Hapeshi, D. Fatta-Kassinos, I. Poulios, Solar-induced heterogeneous photocatalytic degradation of methylparaben. Appl. Catal. B Environ. **178**, 2–11 (2015). https://doi.org/10.1016/j.apcatb.2014.11.022